

Constraints on Relativistic Jets in Quiescent Black Hole X-ray Binaries from Broadband Spectral Modeling

Richard M. Plotkin,^{1*} Elena Gallo,¹ Sera Markoff,² Jeroen Homan,³ Peter G. Jonker,^{4,5,6} James C. A. Miller-Jones,⁷ David M. Russell,⁸ and Samia Drappeau⁹

¹*Department of Astronomy, University of Michigan, 1085 South University Avenue, Ann Arbor, MI 48109*

²*Anton Pannekoek Institute for Astronomy, University of Amsterdam, Science Park 904, 1098 XH, Amsterdam, the Netherlands*

³*Kavli Institute for Astrophysics and Space Research, Massachusetts Institute of Technology, 70 Vassar Street, Cambridge, MA 02139, USA*

⁴*SRON, Netherlands Institute for Space Research, Sorbonnelaan 2, 3584-CA, Utrecht, The Netherlands*

⁵*Department of Astrophysics/IMAPP, Radboud University Nijmegen, Heyendaalseweg 135, 6525-AJ, Nijmegen, The Netherlands*

⁶*Harvard-Smithsonian Center for Astrophysics, 60 Garden Street, Cambridge, MA 02138, USA*

⁷*International Centre for Radio Astronomy Research, Curtin University, G.P.O. Box U1987, Perth, WA 6845, Australia*

⁸*New York University Abu Dhabi, PO Box 129188, Abu Dhabi, UAE*

⁹*Institut de Recherche en Astrophysique et Planétologie (IRAP), 9 avenue du Colonel Roche, BP 44346-31028, Toulouse, France*

ABSTRACT

The nature of black hole jets at the lowest detectable luminosities remains an open question, largely due to a dearth of observational constraints. Here, we present a new, nearly-simultaneous broadband spectrum of the black hole X-ray binary (BHXB) XTE J1118+480 at an extremely low Eddington ratio ($L_X \sim 10^{-8.5} L_{\text{Edd}}$). Our new spectral energy distribution (SED) includes the radio, near-infrared, optical, ultraviolet, and X-ray wavebands. XTE J1118+480 is now the second BHXB at such a low Eddington ratio with a well-sampled SED, thereby providing new constraints on highly sub-Eddington accretion flows and jets, and opening the door to begin comparison studies between systems. We apply a multi-zone jet model to the new broadband SED, and we compare our results to previous fits to the same source using the same model at 4–5 decades higher luminosity. We find that after a BHXB transitions to the so-called quiescent spectral state, the jet base becomes more compact (by up to an order of magnitude) and slightly cooler (by at least a factor of two). Our preferred model fit indicates that jet particle acceleration is much weaker after the transition into quiescence. That is, accelerated non-thermal particles no longer reach high enough Lorentz factors to contribute significant amounts of synchrotron X-ray emission. Instead, the X-ray waveband is dominated by synchrotron self-Compton emission from a population of mildly relativistic electrons with a quasi-thermal velocity distribution that are associated with the jet base. The corresponding (thermal) synchrotron component from the jet base emits primarily in the infrared through ultraviolet wavebands. Our results on XTE J1118+480 are consistent with broadband modeling for A0620-00 (the only other comparably low Eddington ratio BHXB with a well-sampled SED) and for Sgr A* (the quiescent supermassive black hole at the Galactic center). The above could therefore represent a canonical baseline geometry for accreting black holes in quiescence. We conclude with suggestions for future studies to further investigate the above scenario.

Key words: acceleration of particles — accretion, accretion discs — stars: individual: XTE J1118+480 — ISM: jets and outflows — X-rays: binaries

1 INTRODUCTION

Both transient black hole X-ray binaries (BHXBs) and supermassive black holes (SMBHs) spend the majority of their time accreting at very low rates relative to their Eddington

* E-mail: rplotkin@umich.edu

luminosities L_{Edd} ,¹ living in the so-called quiescent regime. For BHXBs, we define quiescence as an X-ray luminosity $L_X \lesssim 10^{-5} L_{\text{Edd}}$, corresponding to $\lesssim 10^{34} \text{ erg s}^{-1}$ for an $8.5 M_\odot$ black hole (see Plotkin, Gallo & Jonker 2013). There is general agreement that quiescent black holes accrete predominantly from some form of a radiatively inefficient accretion flow (RIAF), with X-rays emitted by a population of hot electrons. However, there are still several open questions regarding the nature of accretion flows at such low Eddington ratios. For instance, there is significant debate on whether the hot electrons are primarily thermal or non-thermal, and if they are mostly inflowing or outflowing (e.g., McClintock et al. 2003). Largely limiting our understanding is that it is unknown if quiescent black holes always launch steady collimated jets. Therefore, current accretion models are poorly constrained regarding the degree to which jets are important, both in terms of particle acceleration and the bulk flow of the jet plasma.

Given the low flux levels of quiescent black holes, an inherent challenge is that even the best multiwavelength datasets generally have relatively low signal-to-noise. A natural starting point therefore is to extrapolate trends observed at slightly higher accretion rate for “hard state” BHXBs ($\sim 10^{-5} \lesssim L_X \lesssim 10^{-2} L_{\text{Edd}}$; see, e.g., Remillard & McClintock 2006; Belloni 2010 for reviews on BHXB spectral states), for which higher-quality data exists for a larger number of sources. The dominant X-ray emission mechanism in the hard state is still under debate. For example, for the inflowing component, there can be a contribution from a RIAF (e.g., Remillard & McClintock 2006) and/or an efficient thin disk (e.g., Miller et al. 2006; Wilkinson & Uttley 2009; Reis, Fabian & Miller 2010; Reynolds & Miller 2013), and the relative balance between the two types of flows might not be universal for every source. Regardless, it is well-established that hard state BHXBs are associated with compact radio emission, which is interpreted as optically thick synchrotron radiation from the partially self-absorbed flat spectral component of a compact relativistic jet (Blandford & Königl 1979; Hjellming & Johnston 1988; Fender 2001). The compact jet typically remains unresolved in the radio, except for in a handful of cases with high (very long baseline interferometric) spatial resolution imaging (e.g., GRS 1915+105; Cyg X-1; Dhawan, Mirabel & Rodríguez 2000; Stirling et al. 2001). The compact jet becomes optically thin around near-infrared (NIR) frequencies ($\sim 10^{12}$ – 10^{14} Hz; Corbel & Fender 2002; Russell et al. 2013), and synchrotron radiation from this optically thin component can sometimes extend into the X-ray waveband (e.g., Markoff, Falcke & Fender 2001; Markoff et al. 2003; Russell et al. 2010, 2013). Besides emitting high-energy radiation, the jet might also carry away the bulk of the accretion power via mechanical energy (e.g., Fender, Gallo & Jonker 2003; Gallo et al. 2005, and references therein). In short, the apparent trend is that the jet becomes increasingly important in the hard state as Eddington ratio decreases.

¹ The Eddington luminosity is the limit above which radiation pressure halts the accretion of material onto the black hole, corresponding to $L_{\text{Edd}} = 1.26 \times 10^{38} [M/M_\odot] \text{ erg s}^{-1}$ for ionized hydrogen in a spherical geometry, where M is the black hole mass.

A major outstanding question is if the increasing importance of the jet extends all the way into quiescence. For example, it is well-known that quiescent BHXBs have softer X-ray spectra than hard state systems (e.g., Kong et al. 2002; Tomsick et al. 2003; Corbel, Tomsick & Kaaret 2006; Corbel, Koerding & Kaaret 2008; Plotkin, Gallo & Jonker 2013; Reynolds et al. 2014). However, multiple accretion scenarios can explain the X-ray spectral softening comparably well given the available (low signal-to-noise) data. It is thus not understood if the softer X-ray spectra actually signify a switch in accretion properties, or if the accretion flow and jet simply evolve toward a ‘baseline’ as a BHXB approaches the quiescent state (see Plotkin, Gallo & Jonker 2013, for details). Further hindering our understanding is the challenge of routinely obtaining multiwavelength detections for quiescent BHXBs, largely due to the very low flux levels of these systems. It is therefore not clear if relativistic jets always persist deep into quiescence in the first place. For example, only two quiescent BHXBs have reliable radio detections: V404 Cyg ($L_X \sim 10^{-6} L_{\text{Edd}}$; Hjellming et al. 2000; Gallo, Fender & Hynes 2005) and A0620-00 ($L_X \sim 10^{-8.5} L_{\text{Edd}}$; Gallo et al. 2006). Miller-Jones et al. (2011) performed a deep radio survey that included 11 BHXBs in quiescence, none of which was detected in the radio. They demonstrated that if other quiescent BHXBs launch jets with powers and radiative efficiencies as expected from extrapolating the hard state trends into quiescence, then we can expect to detect jet radio emission only from a select number of very nearby systems, even with our most sensitive radio telescopes.

Given these challenges, some of our best insight into quiescent black holes so far has come from multiwavelength studies of Sgr A*, the compact radio source associated with the $\sim 4 \times 10^6 M_\odot$ SMBH at the Galactic center ($L_X \sim 10^{-11} L_{\text{Edd}}$). Falcke & Markoff (2000) applied a relativistic jet model to the broadband spectral energy distribution (SED) of Sgr A*, to investigate if its flat radio spectrum could signify the presence of a compact self-absorbed synchrotron jet (Blandford & Königl 1979). They concluded that if the radio emission is optically thick synchrotron from a compact jet, then the fraction of particles in the jet that are accelerated into a non-thermal power-law tail must be very small. The primary constraint leading to this conclusion is that the observed infrared (IR) spectrum implies an underlying lepton spectrum that is too steep (power law index $p > 3.8$) to result from standard particle acceleration scenarios ($p = 2.0 - 2.4$; e.g., Drury 1983). The underlying particles are thus predominantly in a quasi-thermal distribution, with only a small fraction of non-thermal particles present. However, Sgr A* undergoes approximately daily X-ray flares that typically last for ~ 1 hour. During these flares, the X-ray spectrum hardens and a non-thermal radiation component emitted from within the inner few gravitational radii dominates over the quiescent X-ray emission. Broadband spectral modeling favors scenarios where the non-thermal X-ray radiation during the flares is synchrotron emission from non-thermal leptons, likely due to sporadic particle acceleration events (Markoff et al. 2001; Dodds-Eden et al. 2009; Dibi et al. 2014).

The above results for Sgr A* suggest a picture where quiescence is associated with only weak, and possibly sporadic, particle acceleration in the jets. The emission prop-

erties of Sgr A* when it is flaring appear to be analogous to those of hard state BHXBs (Markoff 2005), perhaps indicating that such a scenario might also be applicable to BHXBs as well. However, our knowledge on the emission mechanism(s) from BHXBs that are analogous to Sgr A* when it is not flaring is currently rather limited. Almost all of our observational constraints on very low luminosity BHXBs ($L_X \sim 10^{-8.5} L_{\text{Edd}}$) are derived from A0620-00, because it is the only one with a well sampled SED from the radio through the X-ray wavebands.² Interestingly, broadband modeling of A0620-00 in quiescence indeed supports the idea of quiescent emission properties similar to Sgr A* (Gallo et al. 2007). However, we cannot determine from a single source if such a trend applies to all BHXBs. Furthermore, A0620-00 has been in quiescence for over 30 years (and multiwavelength coverage of its previous outburst naturally pales in comparison to today's standards). So pending a future outburst, it is impossible to directly compare its quiescent and hard state properties in detail.

There is a strong need for additional well-sampled SEDs of quiescent BHXBs. To this aim, we recently obtained new coordinated *Chandra* X-ray, *SWIFT* ultraviolet (UV), William Herschel Telescope optical and NIR, and Karl G. Jansky Very Large Array (VLA) radio observations of the BHXB XTE J1118+480 (hereafter J1118). Given its nearby and well-constrained distance of 1.72 ± 0.10 kpc (Gelino et al. 2006) and high Galactic latitude ($b = +62^\circ$; meaning that the amount of line of sight absorption is small), J1118 is one of the few known BHXBs for which it is possible to simultaneously detect both radio and X-ray emission in quiescence. Indeed, our new VLA observation yielded the lowest-luminosity radio detection of a BHXB jet to date (Gallo et al. 2014). With an Eddington ratio of $L_X/L_{\text{Edd}} \sim 10^{-8.5}$, J1118 is one of our best probes of black hole accretion flows at the lowest detectable luminosities. A special aspect of J1118 is that it has also been well-studied at higher luminosities during previous outbursts (e.g., Esin et al. 2001; Markoff, Falcke & Fender 2001; McClintock et al. 2001; Hynes et al. 2000, 2003; Chaty et al. 2003; Malzac, Merloni & Fabian 2004; Yuan et al. 2005; Zurita et al. 2006; Maitra et al. 2009; Brocksopp et al. 2010; Vila et al. 2012; Zhang & Xie 2013).

In this paper, we apply a multi-zone jet model to our newly-assembled broadband SED of J1118 in quiescence. The same model employed here has also been applied to J1118 in the hard state (Maitra et al. 2009), and also to A0620-00 in quiescence ($10^{-8.5} L_{\text{Edd}}$; Gallo et al. 2007), providing a unique opportunity to *uniformly* compare potential changes in accretion and jet properties as a function of Eddington ratio within an individual source as well as to another quiescent BHXB. Here, we focus on the spectral modeling of these data, and we discuss these data in the context of radio/X-ray luminosity correlations in a companion paper (Gallo et al. 2014). In Section 2 we describe our observations and data reduction, where we add nearly simultaneous NIR, optical, and UV observations to the VLA radio and

Chandra X-ray data points. A summary of the jet model is included in Section 3. Results from our best model-fit are presented in Section 4, which are then discussed in Section 5. Throughout, we adopt the following parameters for J1118: black hole mass $M_{\text{BH}} = 7.5 M_\odot$, orbital inclination $i = 68^\circ$ (Khargharia et al. 2013), and distance $d = 1.72 \pm 0.10$ kpc (Gelino et al. 2006). The orbital period is $P_{\text{orb}} = 4.08(\pm 5 \times 10^{-6})$ h (Torres et al. 2004). We adopt a Galactic extinction of $A_V = 0.065$ mag toward J1118 (Gelino et al. 2006), and a Cardelli, Clayton & Mathis (1989) reddening law in the NIR through UV. For X-ray absorption, we use $N_{\text{H}} = 1.2 \times 10^{20} \text{ cm}^{-2}$ (McClintock et al. 2003). The high Galactic latitude of J1118 means that its SED is virtually unabsorbed (see, e.g., McClintock et al. 2003), and our model results are not sensitive to the exact values adopted for A_V and N_{H} . All error bars on X-ray measurements and best-fit parameters are quoted at the 90% confidence level, unless stated otherwise. Uncertainties on flux densities at other wavebands are quoted at the 1σ level.

2 OBSERVATIONS

Here, we describe the nearly simultaneous radio, NIR, optical, UV, and X-ray observations that comprise our new SED of J1118 in quiescence. Details on the *Chandra* X-ray and VLA radio observations, which were taken through a joint *Chandra*/NRAO program during *Chandra* Cycle-14 (PI Gallo, Proposal 14400368), are described by Gallo et al. (2014). We only briefly summarize those observations and data here, and we describe our observations at the other wavebands in more detail. We also include non-simultaneous IR data from Spitzer and the Wide-field Infrared Survey Explorer (WISE; Wright et al. 2010) in our SED to improve the spectral coverage (see Section 2.2.3). The observations and measured flux densities in each waveband (before applying any extinction correction) are summarized in Table 1.

2.1 Summary of Radio and X-ray Observations

We observed J1118 in the radio with the VLA in the C configuration (angular spatial resolution of $\sim 4''$) in two overlapping 1024-MHz base bands centered at frequencies of 4.8 and 5.8 GHz. The observations were split over two days, 2013 June 27 and 28, yielding a total of 11.3 h on source. The data were reduced following standard procedures with the Common Astronomy Software Application (CASA; McMullin et al. 2007) v4.1.0. Data from each day were reduced and imaged separately, and then combined to create a single deep image. A 3.2σ peak was detected in the combined radio image, coincident with the expected position of J1118. To improve the S/N , we added 2.4h of integration time on source from an archival observation from 2010 November. J1118 has a radio flux density of $4.79 \pm 1.45 \mu\text{Jy beam}^{-1}$, which corresponds to a radio luminosity of $\nu L_\nu = 9.83 \times 10^{25} \text{ erg s}^{-1}$ at 5.3 GHz (assuming a flat radio spectrum).

The *Chandra* X-ray observation was taken on 2013 June 27 (obsID 14630), with a net exposure time of 58 ks. The target was placed at the aim point of the S3 chip on the Advanced CCD Imaging Spectrometer (ACIS; Garmire et al.

² We note that the SED of V404 Cyg has also been well sampled in quiescence (Hynes et al. 2009), but its quiescent X-ray luminosity is approximately two orders of magnitude higher than A0620-00.

2003). The data were reduced following standard procedures with the Chandra Interactive Analysis of Observations (CIAO) software, v4.5 (Fruscione et al. 2006). We obtain a total of 146 counts within a circular source aperture centered on the X-ray source position (with radius = $3''$), with an expected 15 of those being background counts (as estimated from a circular annulus with inner and outer radii of 10 and $30''$, respectively). The net count rate is $(2.3 \pm 0.3) \times 10^{-3}$ counts s^{-1} . Assuming a power-law with photon index³ $\Gamma = 2$ (see Section 4), the absorbed 0.5–7 keV flux is $1.46(\pm 0.22) \times 10^{-14}$ erg s^{-1} cm^{-2} . In order to perform the broadband spectral fitting (which is done in X-ray detector space; see Section 4), we extract an X-ray spectrum with the CIAO tool `specextract`. We also create a response matrix file (rmf) and auxiliary response file (arf), applying an energy-dependent point source aperture correction to the arf to account for the $3''$ source aperture.

2.2 Observations at Other Wavebands

2.2.1 Near-infrared and Optical

We obtained NIR and optical observations of the counterpart to J1118 using the 4.2 m William Herschel Telescope (WHT) on La Palma (Spain). We employed two instruments, the Long-slit Intermediate Resolution Infrared Spectrograph (LIRIS) and the auxiliary port camera (ACAM), both in their imaging mode. Observations were obtained on 2013 June 27 and 28, where we obtained images in the K_s , H, J, Sloan i' , r' , and g' filters on both nights.

For the NIR observations taken with LIRIS, we applied a 9-point dither pattern where we took two exposures of 30 s each at all of the 9 positions in the K_s band, one exposure of 20 s at each position in the H-band, and one exposure of 30 s at each position in the J-band. Routines from the LIRIS data reduction pipeline THELI (Schirmer 2013) were used to correct for the sky background and flatfield. Using information from the Two Micron All Sky Survey (2MASS; Skrutskie et al. 2006) on the position of sources detected in the individual frames, these separate frames were averaged such that we obtained two separate images of J1118 in each filter per night. We obtained a photometric calibration by using several unsaturated stars in the LIRIS field of view that are detected in the 2MASS catalog.

For the optical ACAM observations we acquired three exposures in each filter with exposure times of 240 s, 120 s, and 120 s for the g' , r' , and i' filters, respectively. We applied standard data reduction techniques using IRAF to correct for the bias and flatfield. We combined the three images per filter to reduce the statistical error of each measurement. For the photometric calibration we used g' , r' , and i' magnitudes of several stars in the field as reported in the Sloan Digital Sky Survey (SDSS; York et al. 2000).

For each image, we list the flux densities at the effective wavelength of each filter in Table 1 (one image per night in g' , r' , and i' ; two images per night in J, H, and K_s). The

differences in the flux densities within each filter are consistent with the expected degree of periodic variability due to orbital modulations of the secondary star. To incorporate this systematic into the broadband spectral fitting, we use the average flux density for each of the six filters over both nights (after correcting for Galactic extinction), and then we add systematic error bars to each of the six data points at the $\pm 15\%$ level (the amplitude of the orbital modulations are typically ± 0.15 – 0.20 mag; Gelino et al. 2006).

2.2.2 Ultraviolet

We observed J1118 on 2013 June 27 with the *Ultraviolet/Optical Telescope* (UVOT; Roming et al. 2005) onboard *SWIFT* (Gehrels et al. 2004), using the uvw1 (1554 s), uvm2 (1428 s), and uvw2 (1554 s) filters (PI Homan). Individual frames were combined using the tool `uvotimsum`. In the combined images, a source was detected at the expected target position at the 2.9, 4.1, and 1.9σ levels in the uvw1, uvm2, and uvw2 filters, respectively. We consider J1118 to be detected in the uvw2 filter (even though it is only at the 1.9σ level) because it is coincident with the expected target position, and the source can be seen when visually inspecting the images. Using the tool `uvotsource`, we obtain flux density measurements of 3.99 ± 0.99 (uvw1), 2.24 ± 0.78 (uvm2), and 1.15 ± 0.61 μ Jy (uvw2) at each filter’s effective wavelength (2600, 2246, and 1928 Å, respectively). The systematic errors in the uvw1, uvm2, and uvw2 filters are ± 0.12 , 0.01, 0.02 μ Jy, respectively. We correct each flux density for Galactic extinction, using the A_λ/A_V ratios tabulated in Kataoka et al. (2008).

2.2.3 Non-simultaneous Infrared Data

J1118 appears in the all-sky data release of WISE, which surveyed the entire infrared (IR) sky in four filters in 2010. J1118 was detected in the W1 (3.4μ m) and W2 (4.6μ m) filters, with flux densities of 85 ± 6 ($S/N=18.6$) and 79 ± 12 μ Jy ($S/N=9.2$), respectively. There was no detection in the W3 (12μ m) and W4 (22μ m) filters, for which we adopt the 95% confidence flux upper limits listed in the WISE catalog. We also include archival infrared (IR) observations from the *Spitzer Space Telescope* (PI: M. Muno; program 3289). J1118 was observed on 2004 Nov 21 with the Infrared Array Camera (IRAC; Fazio et al. 2004) and detected in both the 4.5 and 8.0μ m bands. J1118 was also observed, but not detected, in the 24μ m band with the Multiband Imaging Photometer for *Spitzer* (MIPS; Rieke et al. 2004) on 2005 May 13 (Muno & Mauerhan 2006). We adopt flux densities of 69 (4.5μ m) and 59 μ Jy (8.0μ m), and an upper limit of < 50 μ Jy at 24μ m, as measured by Gallo et al. (2007) who analyzed the same data originally presented in Muno & Mauerhan (2006). Gallo et al. (2007) estimated that the statistical uncertainties in the flux densities are at the 10% level.

Quiescent BHXBs are known to experience a low-level of flux variability (e.g., Khargharia et al. 2013; Shahbaz et al. 2013; Bernardini & Cackett 2014, and references therein). Muno & Mauerhan (2006) estimate that a level of flux variability in the IR of $\sim 30\%$ could be reasonable. From the overlap between the *Spitzer* 4.5μ m band and the WISE W2 filter observations, we find a $\sim 15\%$ dif-

³ The X-ray photon index Γ is defined as $N(E) = N_0(E/E_0)^{-\Gamma}$, where $N(E)$ is the number of photons at a given energy E , N_0 is the photon number normalization, and $E_0 = 1$ keV is the reference energy.

Table 1. Observing Log and SED

Date	Start Time ^a (UTC)	Telescope	Filter	Frequency (Hz)	Flux Dens. ^b (μJy)	A_λ ^c (mag)
Nearly Simultaneous Observations						
2013 June 27-28	21:30	VLA	C-band	5.3×10^9	4.79 ± 1.45	
2013 June 27	20:56	WHT/LIRIS	K_s	1.39×10^{14}	111.10 ± 4.58	0.008
2013 June 27	22:15	WHT/LIRIS	K_s	1.39×10^{14}	117.31 ± 4.98	0.008
2013 June 28	20:53	WHT/LIRIS	K_s	1.39×10^{14}	134.44 ± 5.26	0.008
2013 June 28	22:11	WHT/LIRIS	K_s	1.39×10^{14}	128.04 ± 5.33	0.008
2013 June 27	21:26	WHT/LIRIS	H	1.80×10^{14}	123.68 ± 4.33	0.012
2013 June 27	22:30	WHT/LIRIS	H	1.80×10^{14}	133.63 ± 4.97	0.012
2013 June 28	21:26	WHT/LIRIS	H	1.80×10^{14}	151.74 ± 5.01	0.012
2013 June 28	22:25	WHT/LIRIS	H	1.80×10^{14}	166.53 ± 5.70	0.012
2013 June 27	21:33	WHT/LIRIS	J	2.43×10^{14}	128.50 ± 3.63	0.019
2013 June 27	22:37	WHT/LIRIS	J	2.43×10^{14}	125.86 ± 4.14	0.019
2013 June 28	21:33	WHT/LIRIS	J	2.43×10^{14}	125.40 ± 3.48	0.019
2013 June 28	22:32	WHT/LIRIS	J	2.43×10^{14}	148.97 ± 4.29	0.019
2013 June 27	21:45	WHT/ACAM	i'	4.01×10^{14}	87.83 ± 0.89	0.044
2013 June 28	21:44	WHT/ACAM	i'	4.01×10^{14}	80.81 ± 0.67	0.044
2013 June 27	21:54	WHT/ACAM	r'	4.86×10^{14}	78.13 ± 0.57	0.057
2013 June 28	21:51	WHT/ACAM	r'	4.86×10^{14}	66.59 ± 0.48	0.057
2013 June 27	22:04	WHT/ACAM	g'	6.40×10^{14}	39.15 ± 0.31	0.079
2013 June 28	22:01	WHT/ACAM	g'	6.40×10^{14}	32.75 ± 0.37	0.079
2013 June 27	19:49	SWIFT/UVOT	uvw1	1.15×10^{15}	3.99 ± 0.99	0.140
2013 June 27	19:39	SWIFT/UVOT	uvm2	1.34×10^{15}	2.24 ± 0.78	0.152
2013 June 27	19:30	SWIFT/UVOT	uvw2	1.56×10^{15}	1.15 ± 0.61	0.173
2013 June 27	16:11	Chandra	ACIS	0.3-7 keV	$(1.46 \pm 0.22) \times 10^{-14}$	$1.2 \times 10^{20} \text{ cm}^{-2}$
Non-Simultaneous Observations						
2005 May 13		<i>Spitzer</i> /MIPS	24.0 μm	1.25×10^{13}	<50.0	
2010		WISE	22 μm /W4	1.35×10^{13}	<1685.6	
2010		WISE	12 μm /W3	2.68×10^{13}	<214.9	
2004 Nov 21		<i>Spitzer</i> /IRAC	8.0 μm	3.75×10^{13}	59.0 ± 5.9	
2010		WISE	4.6 μm /W2	6.45×10^{13}	78.7 ± 12.2	
2004 Nov 21		<i>Spitzer</i> /IRAC	4.5 μm	6.66×10^{13}	69.0 ± 6.9	
2010		WISE	3.4 μm /W1	8.86×10^{13}	85.0 ± 6.5	

^a UTC is listed only for the nearly simultaneous observations. The VLA observations started at UTC 21:30 on June 27 and at UTC 21:26 on June 28, and they lasted 7.5 h on each day.

^b Flux densities are reported prior to applying corrections for interstellar extinction. For the Chandra observation, we report the absorbed flux from 0.3-7 keV in $\text{erg s}^{-1} \text{cm}^{-2}$, and the quoted uncertainty is at the 90% confidence level (all other error bars are $\pm 1\sigma$).

^c The extinction in each filter is calculated assuming $A_V = 0.065$ mag (Gelino et al. 2006) and a Cardelli, Clayton & Mathis (1989) reddening law with $R_V = 3.1$. For the Swift/UVOT filters, we estimate the extinction using the A_λ/A_V ratios tabulated in Kataoka et al. (2008). For the X-ray, we assume an equivalent Hydrogen absorption column density of $N_H = 1.2 \times 10^{20} \text{ cm}^{-2}$ (McClintock et al. 2003). No extinction correction is applied to the non-simultaneous IR data.

ference in flux between the two IR epochs. We thus conservatively add systematic error bars to all IR data points at the 30% level, in addition to the statistical uncertainties quoted above.

3 MULTI-ZONE JET MODEL

The jet model employed here builds upon earlier foundations for multi-zone jets (e.g., Blandford & Königl 1979; Falcke & Biermann 1995), and it was developed over a series of papers (e.g., Falcke & Markoff 2000; Markoff et al. 2001, 2003; Markoff, Nowak & Wilms 2005; Markoff et al. 2008; Maitra et al. 2009). The earliest motivation was to

study Sgr A* (Falcke & Markoff 2000), with what was a simplified version of the current model. Now, the current model has been applied to several hard state BHXBs and low-luminosity active galactic nuclei (see, e.g., Markoff et al. 2001; Markoff, Nowak & Wilms 2005; Migliari et al. 2007; Markoff et al. 2008; Maitra et al. 2009). Below, we describe essential features of the jet model that are required to understand our current study, and a full description (and history) of the model can be found in Markoff, Nowak & Wilms (2005, and references therein). Throughout, we refer to the model as the MNW05 model, and we adopt the following notation: γ_j refers to the bulk Lorentz factor of the jet plasma; β_e refers to the speeds of radiating electrons, normalized to the speed of light; the corresponding electron

Lorentz factors are $\gamma_e = (1 - \beta_e^2)^{-0.5}$, and their energies are $\gamma_e m_e c^2$ (where m_e is the electron rest mass). All size-scales are normalized to the gravitational radius of the black hole ($r_g = GM_{\text{BH}}/c^2$), unless stated otherwise. We generally use z to refer to the distance of each jet zone from the black hole (the z -axis points along the axis of the jet), and r refers to the radius of each jet zone.

The MNW05 model is for a steady state jet, and it assumes that the radiation is entirely leptonic⁴ and that protons dominate the kinetic energy. The model assumes a maximally dominated jet, which means that the bulk internal energy (dominated by the magnetic field) is comparable to the bulk kinetic energy (dominated by protons; Falcke & Biermann 1995). The total jet power is assumed to scale as $\dot{M}c^2$ at the inner edge of the accretion flow, where \dot{M} is the mass accretion rate. Within each zone of the jet, we calculate the expected flux from synchrotron radiation and SSC, which is then compared to the observed SED of J1118 in quiescence.

The most important free parameter in the jet model is the jet power, N_j , which determines the initial power (normalized to L_{Edd}) that is injected into the electrons and the magnetic field at base of the jet. The very base of the jet has a cylindrical geometry (aligned along the jet axis), with a radius r_0 and height $z = h_0$; we refer to this cylinder as the “nozzle.” The size of the nozzle is controlled by the free parameter r_0 , and we fix the ratio $h_0/r_0 = 1.5$. The radiating particles in the nozzle are assumed to have a quasi-thermal, mildly relativistic (Maxwell-Jüttner) velocity distribution with temperature T_e (T_e in the nozzle is a free parameter). We require $T_e > (m_e c^2)/k_B = 5.94 \times 10^9$ K because we do not consider cyclotron processes. The plasma in the nozzle follows a gas law with an adiabatic index $\Gamma = 4/3$ and has a proper sound speed $\gamma_s \beta_s \sim 0.4$ (i.e., $\beta_s^2 = [\Gamma - 1]/[\Gamma + 1]$). The ratio of energy injected into the nozzle that is initially split between the magnetic field and radiating electrons is controlled by the equipartition factor $k = U_B/U_e$ (k is a free parameter). $U_B = B^2/8\pi$ is the magnetic energy density (where B is the magnetic field), and U_e is the electron energy density (calculated by integrating over the entire electron distribution).

At the top of the nozzle (i.e., $z = h_0$), the jet base is allowed to freely expand laterally, which results in a longitudinal pressure gradient that accelerates the bulk plasma. The bulk flow velocity profile is solved for exactly by the relativistic Euler equation. Note that the conditions in the nozzle (set largely by the free parameters N_j , r_0 , and k), combined with the above adiabatic expansion, sets all macroscopic conditions along the *entire* jet (including the bulk flow velocity, electron temperature, magnetic field, equipartition factor k , and density profiles; see, e.g., Equation 2 of Falcke & Markoff 2000 for analytic forms of some of these profiles). The bulk flow acceleration is weak, typically saturating to $\gamma_j \gtrsim 2 - 3$ in the outer jet.

At some distance from the black hole, z_{acc} , we assume that a significant fraction (60%) of particles in the jet base are accelerated into a non-thermal power-law tail. The acceleration mechanism is unknown, but we assume that it

is related to diffusive shock processes (e.g., Jokipii 1987). The location of the acceleration region is closely related to the location of the jet break frequency, ν_b , in the SED (i.e., the frequency where synchrotron emission turns from optically thick to optically thin). Any optically thin synchrotron (and associated SSC) extending into the X-ray waveband is primarily emitted from this acceleration zone. As one moves into jet zones farther from the black hole, the synchrotron radiation peaks toward lower frequencies, and integrating over the outer zones gives rise to the jet’s signature flat/inverted radio spectrum. We (arbitrarily) integrate to $z_{\text{max}} = 3.2 \times 10^{12}$ cm ($2.9 \times 10^6 r_g$) to save computation time, since jet zones at larger distances contribute radiation predominantly at frequencies below our VLA radio data point at 5.3GHz.

Since the details of the particle acceleration are unknown, we take a heuristic approach to modeling the non-thermal tail of electrons at $z > z_{\text{acc}}$. We simply assume that the non-thermal electrons follow a power-law distribution with index p (i.e., $N(\gamma_e) \propto \gamma_e^{-p}$). To maintain this power law against cooling losses, we assume a constant rate of particle acceleration, t_{acc}^{-1} . We parameterize the microphysics of particle acceleration with the free parameter $\epsilon_{\text{sc}} = \beta_{\text{sh}}^2/\xi$, where β_{sh} is the relative shock velocity (in the shock frame) and ξ is the ratio of the scattering mean free path to the gyroradius (see, e.g., Markoff et al. 2008; Maitra et al. 2009). The free parameter ϵ_{sc} is proportional to the particle acceleration rate (see Markoff, Falcke & Fender 2001):

$$t_{\text{acc}}^{-1} = \frac{3}{4} \epsilon_{\text{sc}} \frac{eB}{\gamma_e m_e c} \quad (1)$$

where e is the electron charge and B is the magnetic field strength at the location of the acceleration zone (all variables are in cgs units).

The minimum particle energy of the non-thermal power law tail is set to the peak of the Maxwell-Jüttner distribution, according to $\gamma_{e,\text{min}} = 2.23 k T_{e,\text{acc}} / (m_e c^2)$, where $T_{e,\text{acc}}$ is the electron temperature at z_{acc} . The maximum particle energy, set by $\gamma_{e,\text{max}}$, is determined by the electron energy where the particle acceleration rate (t_{acc}^{-1}) is balanced by cooling losses. Three sources of cooling losses are considered: (adiabatic) cooling from particles escaping the jet zone (t_{esc}^{-1}), synchrotron cooling (t_{syn}^{-1}), and cooling from inverse Comptonization (t_{com}^{-1}):

$$t_{\text{esc}}^{-1} = \beta_e c / z, \quad (2)$$

$$t_{\text{syn}}^{-1} = \frac{4}{3} \sigma_T \gamma_e \beta_e^2 \frac{U_B}{m_e c}, \quad (3)$$

where σ_T is the Thomson cross section and U_B is the magnetic energy density at z_{acc} , and

$$t_{\text{com}}^{-1} = t_{\text{syn}}^{-1} \frac{U_{\text{rad}}}{U_B}, \quad (4)$$

where U_{rad} is the energy density of the incident radiation providing the seed photons for inverse Comptonization. Thus, $\gamma_{e,\text{max}}$ is found by solving $t_{\text{acc}}^{-1} = t_{\text{esc}}^{-1} + t_{\text{syn}}^{-1} + t_{\text{com}}^{-1}$. The cutoff frequency of non-thermal synchrotron radiation in the broadband spectrum is related to the values of $\gamma_{e,\text{max}}$ and B in the acceleration zone through $\nu_{\text{cut}} = 0.29 \nu_{\text{crit}}$, where

⁴ Throughout the text, we will assume that the leptons are electrons for convenience.

$\nu_{crit} = 3/(4\pi)\gamma_{e,max}^2(eB)/(m_e c)$ is the critical synchrotron frequency. The MNW05 model assumes that the cooling rate is dominated by adiabatic losses. This assumption is important to keep in mind when interpreting our best-fits to the SED of J1118.

We refer to the combination of all jet zones closer to the black hole than the acceleration region ($z < z_{acc}$) as the “jet base”, and we refer to regions of the outer jet at $z > z_{acc}$ as “post-accelerated” zones. The “nozzle” refers only to the cylindrical component (at $z < h_0$) that is not freely expanding. We stress that the particle distributions within the post-accelerated zones contain a combination of both thermal and non-thermal particles, while the jet base only contains a thermal component. In each zone, the electron temperature ($T_e[z]$) and the minimum/maximum Lorentz factors ($\gamma_{e,min/max}[z]$) describing the power-law tail (in the post-acceleration regions) are adjusted to lower values as one moves away from the black hole, following the prescription set by the adiabatic expansion of the bulk plasma flow (we again note that the bulk flow is controlled only by the conditions in the nozzle and the adiabatic expansion beginning at $z = h_0$).

As input to the model, we also include the following properties of the BHXB system: black hole mass (M_{BH}), distance (d), orbital inclination (i), and the equivalent Hydrogen line of sight absorbing column (N_H), which we fix to the parameters listed at the end of Section 1. The companion star to J1118 is known to have a late-type spectral class (Khargharia et al. 2013). So we include a blackbody component at a fixed temperature $T_* = 3400$ K, and we normalize this component by assuming an emitting sphere with radius $R_* = 0.56 R_\odot$. This blackbody component contributes to $\sim 90\%$ of the total observed flux in each NIR filter, and ~ 25 , 40 , and 70% of the total flux in the Sloan g' , r' , and i' filters, respectively, consistent with the expected contribution of the secondary from Gelino et al. (2006).

Finally, we do not include any thermal emission from a standard geometrically thin accretion disk, which in turn implies that there is no source of seed photons for external inverse Compton scattering. Thus, all modeled inverse Comptonisation processes are synchrotron self-Compton (SSC).⁵ Given the observed quiescent X-ray flux of J1118, any thin disk must be relatively cool with an inner disk temperature $kT_{in} \lesssim 85$ eV (generously assuming that the total observed X-ray flux accounts for only 1% of the bolometric disk luminosity and a maximally spinning prograde black hole, and including a color correction term; see Kubota et al. 1998). Thus, even if a thin disk can persist close to the innermost stable circular orbit in quiescence, we do not have sufficient data to constrain its properties: the blackbody emission would likely peak between the SWIFT UV and *Chandra* X-ray data points, and we do not observe a sufficient number of X-ray photons to detect a soft thermal excess or reflection signatures like an Iron $K\alpha$ line. We similarly cannot accurately constrain any contribution of (optical) thermal radiation from the outer regions of the accretion disk, pri-

marily due to the relative brightness of the companion star and the sampling of our SED. We discuss these limitations in Section 5.

3.1 Notes on fixed and free jet model parameters

The MNW05 model includes several input parameters, which are summarized in the notes to Table 2. We also note in Table 2 which parameters are fixed during the model fitting, the majority of which are constrained from observations of J1118 (e.g., M_{BH} , d , i , N_H , etc.). There are degeneracies among certain sets of remaining parameters, however. These degeneracies can be difficult to disentangle when performing the model fits, especially at the low flux levels observed for J1118 in quiescence. However, from our experience fitting this jet model to other accreting black hole systems, we have found that certain parameters tend to converge toward similar values regardless of the system being modeled (at least in the hard state), including, e.g., Cyg X-1 and GX 339-4 (Markoff, Nowak & Wilms 2005; Maitra et al. 2009), GRO J1655-40 (Migliari et al. 2007), and even supermassive black holes like M81* (Markoff et al. 2008).

For J1118 in quiescence, we therefore fix the ratio of the nozzle height to radius (h_0/r_0) to 1.5, and the fraction of thermal particles accelerated into the non-thermal tail in the acceleration region to 0.6. These values are similar to values found for other systems, and most importantly are consistent with values found and/or adopted by the Maitra et al. (2009) fits of the MNW05 model to J1118 in the hard state (easing our goal of comparing J1118 in quiescence and the hard state). If we were to adopt other values for these two parameters, then the remaining free model parameters would compensate to yield a fit of comparable statistical quality. However, the broad, qualitative features of the fit would remain identical (and quantitatively, the best-fit parameters are generally fairly similar within the uncertainties on each parameter). Therefore, as summarized in Table 2, the main jet model parameters we explore here are the jet power (N_j), the equipartition at the base of the jet (k), the radius of the nozzle (r_0), the electron temperature in the nozzle (T_e), the particle acceleration rate (parameterized by ϵ_{sc}), the location of the particle acceleration zone (z_{acc}), and the accelerated particle power law index (p).

4 RESULTS

Before performing detailed modeling, we first confirm that the X-ray spectrum is typical for a quiescent BHXB by fitting just the X-ray spectrum with a (phenomenological) power law modified by Galactic absorption (N_H is fixed to the value in Section 1). The X-ray spectrum is fit within the Interactive Spectral Interpretation System (ISIS; Houck & Denicola 2000) v1.6.2-10 using Cash statistics (Cash 1979), and we find a best-fit photon index $\Gamma = 2.02 \pm 0.41$. This photon index is consistent with other quiescent BHXBs (Plotkin, Gallo & Jonker 2013), and nearly identical to a 2002 *Chandra* observation of J1118 in quiescence ($\Gamma = 2.02 \pm 0.16$; McClintock et al. 2003). With this photon index and our adopted values for N_H and distance, we estimate an intrinsic (i.e., unabsorbed) 1-10 keV

⁵ SSC is calculated in every zone. In practice though, the SSC emission turns out to come predominantly from zones toward the bottom of the jet base, since the photon field and electron densities are highest at those locations.

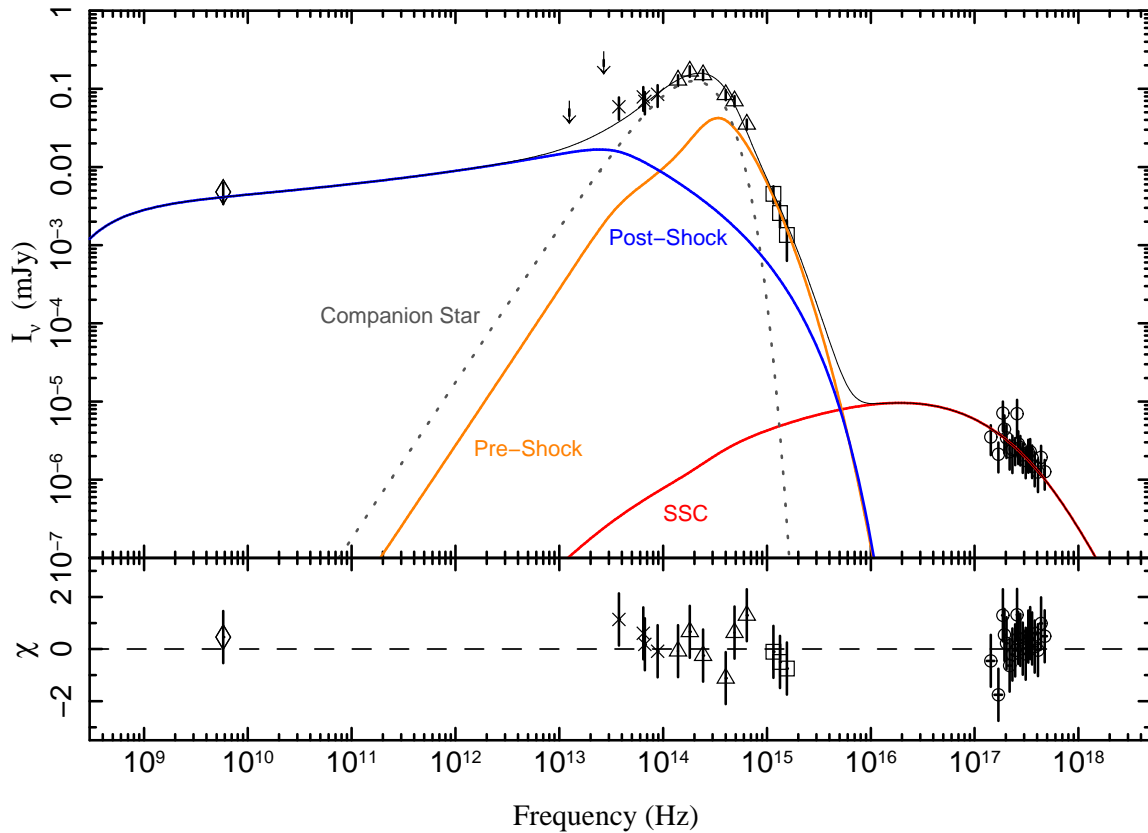


Figure 1. Broadband spectrum and best-fit model. Symbols are for the radio (diamond), (non-simultaneous) IR (arrows for upper limits; crosses for detections), NIR and optical (triangles), UV (squares), and X-ray (circles) data points. The jet model is fit in X-ray detector space, with the best-fit shown with the black solid line. Also shown are the contribution from the pre-shock (thermal) synchrotron emission (orange line), the post-shock (non-thermal) synchrotron emission (blue line), SSC (red line), and the companion star (dotted black line).

X-ray luminosity of $L_X = 4.5 \times 10^{30} \text{ erg s}^{-1}$ using the Chandra Portable, Interactive Multi-Mission Simulator (PIMMS; Mukai 1993). The implied Eddington ratio is $(L_X/L_{\text{Edd}}) = 10^{-8.5}$.

Next, we fit the jet model to the broadband spectrum described in Section 2. An important feature of the model is that the predicted spectrum is forward folded through the X-ray response, and the fit is performed within ISIS. Fitting in “X-ray detector space” allows better control over instrument-related systematics, and also a direct comparison of the goodness of fit via, e.g., χ^2 statistics, at all observed wavelengths in the broadband spectrum. The NIR, optical, and UV data points are corrected for extinction prior to performing the fitting (see A_λ in Table 1), and the X-ray absorption is applied within ISIS during the fit (fixing N_H to our adopted value). We fit the model to the data by minimizing χ^2 (we also try several different sets of initial guess parameters to ensure that the fit is not converging toward a local minimum). The ISIS script `conf_loop` is used to iteratively search for 90% confidence intervals on each free parameter (i.e., $\Delta\chi^2 = 2.71$ for one parameter of interest), and the fit is updated if a better solution is found during the confidence interval search. The fit converges to-

ward small values of ϵ_{sc} , such that the high-energy (post-acceleration) synchrotron cutoff (ν_{cut}) falls below the X-ray waveband. With such a low value of ν_{cut} , it is not possible for the accelerated tail of particles to contribute significant amounts of optically thin synchrotron to the NIR through X-ray wavebands. We therefore cannot constrain the slope of the optically thin synchrotron component from the data, so we instead fix $p = 2.2^6$ and refit the model in order to more tightly constrain the other free parameters.

The best fit to the broadband spectrum is shown in Figure 1, with the best-fit parameters listed in Table 2. Physical parameters calculated by the code (e.g., magnetic field, electron number density, bulk Lorentz factor, etc.) are reported in Table 3, with values listed at the top of the nozzle ($z = h_0$) and at the acceleration zone ($z = z_{\text{acc}}$). We include values

⁶ The spectral index α_ν ($f_\nu \sim \nu^{\alpha_\nu}$) for optically thin synchrotron emission from a power-law distribution of relativistic particles is related to p as $\alpha_\nu = -(p-1)/2$. Similarly, the photon index $\Gamma = (p+1)/2$. A value of $p = 2.2$ is often assumed for compact jet emission. The other best-fit model parameters are not sensitive (within their 90% confidence intervals) to the exact p value chosen from $p = 2 - 3$.

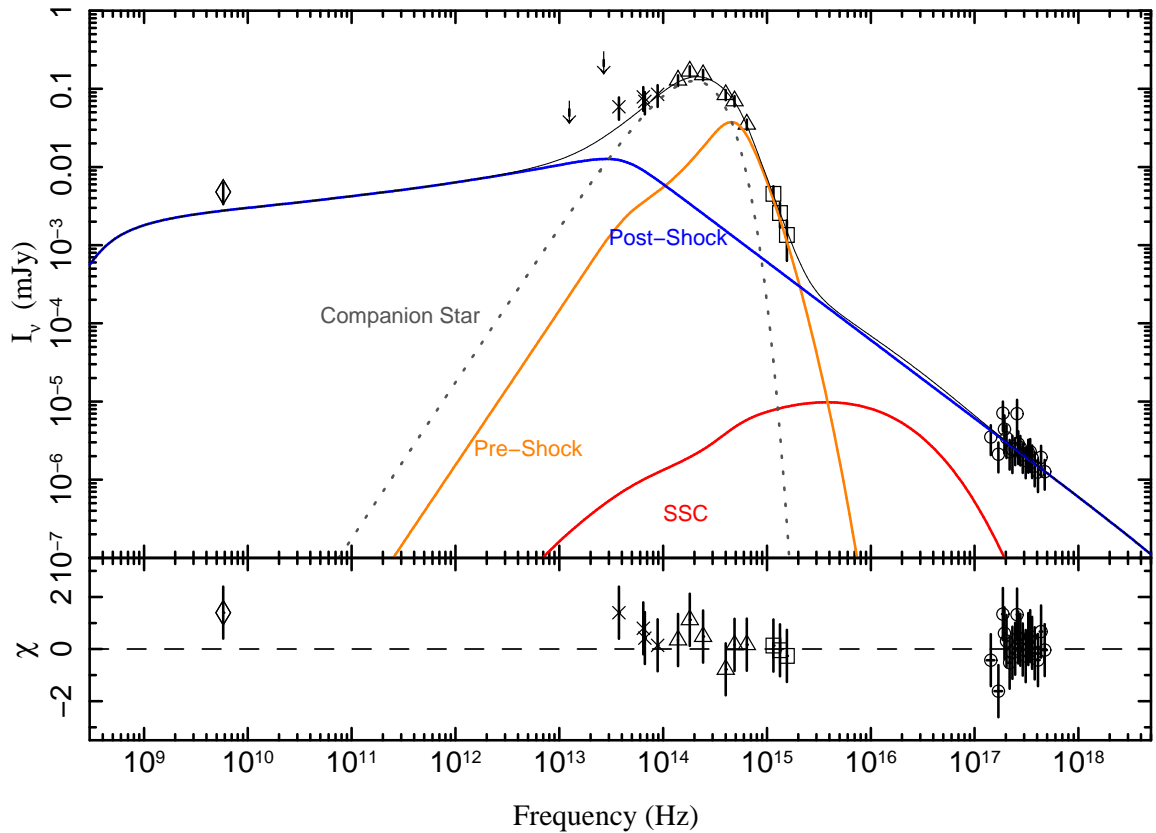


Figure 2. Best-fit model where X-rays are dominated by post-shock (non-thermal) synchrotron emission (see Section 4.1). Symbols and lines have the same meaning as in Figure 1.

in both zones to illustrate how these physical parameters evolve along the jet. We also repeat some key input parameters to the nozzle from Table 2 (e.g., zone radius, electron temperature, etc.), to illustrate how those input parameters evolve along the jet. We obtain a reduced $\chi_r^2 = 0.59$ for 28 degrees of freedom. Since we (somewhat arbitrarily) assign systematic uncertainties to some data points to account for potential variability, we do not necessarily expect χ_r^2 to be close to unity. However, the minimum χ_r^2 still is useful for determining the best-fit *relative* to the searched parameter space, and we also require the fit residuals to not show any obvious trends as a function of frequency upon visual inspection (see bottom panel of Figure 1). We cannot strongly constrain the exact value of ϵ_{sc} from the data, so we report its 95% confidence upper limit in Table 2, which is also the value adopted in Figure 1. We note, however, that our upper limit on ϵ_{sc} is robust, since larger values would allow too much optically thin synchrotron to contribute to the UV and X-ray wavebands, resulting in a poorer statistical fit (although see below). Since the X-ray emission is modeled predominantly by SSC, we refer to this as the SSC-dominated fit.

4.1 Exploring Parameter Space: Synchrotron Dominated X-rays

Since we cannot directly identify the synchrotron cutoff frequency ν_{cut} from the data, we further explore the ϵ_{sc} parameter here. We note that ϵ_{sc} is the only parameter we were not able to adequately investigate from the combination of different sets of initial guess parameters and running `conf_loop` above. We first search for a solution where ν_{cut} falls inside the X-ray band, which would result in both SSC and optically thin synchrotron contributing to the observed X-rays. The model would not converge to such a fit. We also could not find an acceptable fit where ν_{cut} falls between the UV waveband (as in Figure 1) and the soft X-ray waveband.

Next, we explore if the other extreme is possible where X-rays are dominated by optically thin synchrotron radiation emitted by the accelerated (non-thermal) particles. To do so, we force ν_{cut} to fall above the X-ray waveband by (arbitrarily) fixing $\epsilon_{sc} = 0.0025$. In this case, we can directly constrain the spectral slope of the synchrotron emission (emitted by the post-accelerated non-thermal electrons) by using the best-fit X-ray photon index Γ , and we fix $p = 3$. Interestingly, we obtain a fit of similar statistical quality as the above SSC dominated fit, with a reduced $\chi_r^2 = 0.54$ for 29 degrees of freedom (see Figure 2, Table 2, and Table 3). We note that for this ‘synchrotron’-dominated fit, the noz-

Table 2. Best-fit Model Parameters

Parameter (unit)	SSC Dominated Fit	Synchrotron Dominated Fit
N_j ($10^{-5} L_{\text{Edd}}$)	$1.71^{+1.52}_{-0.83}$	$2.67^{+4.55}_{-1.86}$
k	$0.044^{+0.023}_{-0.013}$	$2.066^{+15.829}_{-1.879}$
r_0 (r_g)	$2.3^{+1.2}_{-0.6}$	2.7 ± 0.9
T_e (10^{10} K)	$1.735^{+0.823}_{-0.418}$	$0.611^{+0.286}_{-0.017}$
ϵ_{sc}^a	$< 1.3 \times 10^{-6}$	2.5×10^{-3}
z_{acc} (r_g) ^b	14.4	20.2
p	2.2	3
$\chi^2_r/\text{d.o.f.}$	0.59/28	0.54/29

The table includes the parameter space explored for the MNW05 fits to J1118 in quiescence, and descriptions for each parameter are below (including a summary of all input parameters to the model). The first four parameters describe conditions in the nozzle, while the final three parameters describe the particle acceleration at $z = z_{\text{acc}}$. All parameters in the table are free to vary during the spectral fits, unless stated otherwise below. N_j : power injected into internal energy in the nozzle; k : equipartition factor, equal to the ratio of magnetic energy (U_B) to particle energy (U_e) in the nozzle; r_0 : nozzle radius; T_e : particle temperature in the nozzle; ϵ_{sc} : proportional to the particle acceleration rate t_{acc}^{-1} . $\epsilon_{\text{sc}} = \beta_{\text{sh}}^2/\xi$, where β_{sh} is the relative shock velocity and ξ is the ratio between the scattering mean free path to the gyroradius; z_{acc} : distance of acceleration zone from the black hole; p : power-law index for accelerated leptons ($N_e \sim \gamma_e^{-p}$). p is held fixed to $p = 2.2$ for the ‘SSC’ fit, and $p = 3$ for the ‘synchrotron’ fit (see Section 4); χ^2_r/ν : reduced χ^2 for ν degrees of freedom. We fix the following parameters during the fit: $N_{\text{H}} = 1.2 \times 10^{20} \text{ cm}^{-2}$; black hole mass $M_{\text{BH}} = 7.5 M_{\odot}$; orbital inclination $i = 68^\circ$; distance $d = 1.72 \text{ kpc}$; the ratio of nozzle height to radius (h_0/r_0) = 1.5; the fraction of nozzle particles accelerated into a power-law tail = 0.6; the temperature of the companion star $T_* = 3400 \text{ K}$; and the radius of the companion star $R_* = 0.56 R_{\odot}$. Emission from the jet is calculated out to a distance $z_{\text{max}} = 3.2 \times 10^{12} \text{ cm}$ ($2.9 \times 10^6 r_g$) from the black hole.

^a Limit for SSC fit is at 95% confidence. ϵ_{sc} is held fixed for the synchrotron fit.

^b 90% confidence interval is larger than the allowed range of $10 \leq z_{\text{acc}} \leq 125$.

zle electron temperature T_e is almost non-relativistic (i.e., it is close to the imposed lower boundary in the nozzle, and it becomes non-relativistic at larger distance from the black hole), and the equipartition factor k is poorly constrained. The SSC- and synchrotron-dominated fits are compared in the next section.

5 DISCUSSION

We applied a multi-zone jet model to a new broadband spectrum of J1118 in quiescence ($L_X/L_{\text{Edd}} \sim 10^{-8.5}$), which is only the second BHXB at such a low Eddington ratio to have a radio detection and an SED sampled well enough to attempt broadband modeling. The same model has previously been applied to J1118 in the hard state during its 2000 and 2005 outbursts (Maitra et al. 2009), and also to A0620-00 in quiescence (Gallo et al. 2007). We obtain two model fits for J1118 in quiescence, of comparable statisti-

Table 3. Physical Parameters

Parameter (unit)	SSC-dominated ($z = h_0$) ($z = z_{\text{acc}}$)		Synchrotron-dominated ($z = h_0$) ($z = z_{\text{acc}}$)	
Parameters calculated by model				
B (10^4G)	13.28	2.03	56.42	8.13
n_e (10^{15} cm^{-3})	2.2	0.075	2.2	0.063
γ_j	...	1.72	...	1.73
$\gamma_{e,\text{max}}$...	147	...	17723
Model input parameters				
k	0.044	0.025	2.066	1.811
r (r_g)	2.3	6.5	2.7	8.0
T_e (10^{10}K)	1.735	1.152	0.611	0.403

Parameters calculated by model are reported at the top of the nozzle ($z = h_0$) and at the particle acceleration zone (z_{acc}). *Model input parameters* are key free parameters describing the nozzle. We repeat their best-fit values from Table 2 here, and we also report their values at $z = z_{\text{acc}}$ to illustrate how these parameters change along the jet. B : magnetic field; n_e : number density of electrons in each zone; γ_j : bulk Lorentz factor of the plasma. We do not report a value for γ_j at $z = h_0$ because the plasma has only just begun expanding. γ_j saturates to $\gamma_j \sim 3$ in the outer jet in both the SSC- and synchrotron-dominated fits. $\gamma_{e,\text{max}}$: the maximum electron Lorentz factor after particle acceleration (see §3). No $\gamma_{e,\text{max}}$ is reported at the top of the nozzle because there is no particle acceleration within zones at $z < z_{\text{acc}}$; k : equipartition factor; r : radius of jet zone; T_e : electron temperature of the thermal electron component.

cal quality, that can explain the observed X-rays either as SSC (emitted by a quasi-thermal population of relativistic electrons) or as optically thin synchrotron emission (from an accelerated non-thermal population of electrons). Before describing the physical differences between these two fits, we first discuss their similarities. The origin of X-ray emission from both hard state and quiescent BHXBs is a highly debated topic. However, by highlighting the common features among these two extremes, we can (partly) transcend this debate and obtain fairly robust insight into the nature of jets launched in quiescence.

Both fits converge toward relatively small nozzle radii $r_0 \sim 2 - 3 r_g$. This nozzle radius is smaller than the best-fit values for J1118 in the hard state ($10 - 20 r_g$; Maitra et al. 2009), and comparable to the best-fit value for A0620-00 in quiescence ($3.9^{+2.2}_{-0.1} r_g$; Gallo et al. 2007). When compared to the hard state, both fits also converge toward lower electron temperatures (Maitra et al. 2009 found $T_e \sim 4 \times 10^{10} \text{ K}$). Thus, in the context of this jet model, as a BHXB transitions from the hard state into quiescence, the jet base becomes more compact (perhaps by an order of magnitude), and it evolves toward a lower temperature (by at least a factor of two).

It is interesting that we can explain the bulk of the IR–UV SED with only the combination of emission from the jet and companion star, while completely neglecting any blackbody radiation from the outer regions of the accretion flow. We do not take this result as evidence for the absence of an outer disk, as our reasons for excluding the disk component are largely systematic (see Section 3). An outer disk is likely present, but decomposing its emission from other radiative processes in quiescence likely requires an even better

sampled SED with higher S/N , and/or high-resolution spectroscopy. For example, excess UV emission over the expected contribution from the companion star is often detected from quiescent BHXBs (see Hynes & Robinson 2012 and references therein; although also see Hynes et al. 2009 who did not find a significant UV excess in the relatively luminous quiescent SED of V404 Cyg). Some of this UV excess is likely thermal radiation from the outer disk, as UV spectroscopy often reveals broad emission lines (including for both J1118 and A0620-00; McClintock et al. 2003; Froning et al. 2011). However, a caveat is that explaining typical UV excess fluxes purely via thermal blackbody radiation requires a hotter and/or more compact emission region than expected for the outer regions of quiescent accretion flows (e.g., McClintock, Horne & Remillard 1995; McClintock et al. 2003; Froning et al. 2011; Hynes & Robinson 2012), and complex geometries may be required (e.g., McClintock et al. 2003). Our model fits on J1118 suggest that jet-related synchrotron radiation (from a relativistic population of quasi-thermal electrons in the jet base) could also substantially contribute to the UV waveband and should be taken into account. Note that synchrotron radiation from the jet base can also explain the bulk of the UV excess from A0620-00 in quiescence (Gallo et al. 2007; Froning et al. 2011; although see §4 of Froning et al. 2011 for other potential scenarios).

The NIR and optical wavebands are largely dominated by the companion star in our fits to J1118. However, we find an IR excess (relative to the contribution from the companion star), which we account for as synchrotron radiation predominately from the accelerated (non-thermal) electron component. However, since our IR data points are non-simultaneous, we cannot exclude the possibility that a circumbinary disk may instead contribute to some of the excess IR emission, especially in the Spitzer 8- μ m band (e.g., Muno & Mauerhan 2006; Wang & Wang 2014). If a circumbinary disk is relevant to the IR, then in order to self-consistently also explain the jet radio emission, the jet break (ν_b) would likely need to fall at lower frequencies than in either fit (i.e., the location of the acceleration region, z_{acc} , would be located farther from the black hole; see Gallo et al. 2007). Unfortunately, due to lack of data between the radio and IR wavebands, neither fit constrains z_{acc} to high-precision. Thus, resolving this discrepancy would require higher frequency radio and/or sub-mm observations to better constrain the radio spectral index and to attempt to locate the jet break. Searches for IR variability would also be helpful (the excess IR emission should be variable if it comes from the jet).

5.1 An SSC origin for X-ray emission in quiescence?

Although formally the χ_r^2 values of the SSC- and synchrotron-dominated fits are comparable, we argue here that the SSC-dominated fit is more believable (in the context of the MNW05 model). First, the uncertainties on the best fit parameters N_j and k are especially large for the synchrotron-dominated fit, providing some hesitation on the fit quality. Plus, we obtained the synchrotron-dominated fit by assuming a high particle acceleration rate, i.e., we fixed the parameter $\epsilon_{\text{sc}} \propto t_{\text{acc}}^{-1}$ to a large value. Our motivation for doing so was to help explore the full parameter space, and to

investigate if quiescent black hole jets can efficiently accelerate electrons to high γ_e . However, if we refit the synchrotron-dominated fit and allow ϵ_{sc} to vary as a free parameter, its value does not change significantly, which may suggest that the model simply converged toward a local minimum.

Perhaps more important, and regardless of our above suspicions, the synchrotron-dominated fit also appears to be approaching a parameter space that violates some assumptions behind the MNW05 model. For one, the model assumes a relativistic fluid in the nozzle and jet base, yet the electron temperature in the nozzle for the synchrotron-dominated fit is uncomfortably close to the imposed limit $T_{e,\text{min}} = 5.94 \times 10^9$ K. As the electron temperature follows the adiabatic expansion of the bulk flow, the temperature eventually drops below $T_{e,\text{min}}$ (e.g., see T_e at $z = z_{\text{acc}}$ in Table 3).

Furthermore, the accelerated particles must have a power law index $p \sim 3$ in order to explain the X-ray data. Such a soft particle spectrum is unlikely to be injected by a shock. Therefore, if synchrotron radiation from non-thermal electrons indeed dominates the X-ray waveband in quiescence, then that radiation must be synchrotron cooled (i.e., the synchrotron cooling break, ν_{cool} , lies below the X-ray waveband in quiescence). Below, we confirm that synchrotron cooling losses are unlikely negligible in the X-ray waveband for the synchrotron-dominated fit. To illustrate this point we consider only the acceleration zone (z_{acc}), since the synchrotron flux at high-energies from non-thermal electrons will be largest in this region where the magnetic field is strongest. Electrons in z_{acc} (where $B \sim 8 \times 10^4$ G; see Table 3) that emit synchrotron in the X-ray band ($\approx 2.4 \times 10^{17}$ Hz) have $\gamma_e \approx 1560$. Inserting these numbers into Equations 2–4, we find that synchrotron losses account for 92% of all cooling losses at $\gamma_e \approx 1560$ (adiabatic losses account for the remaining 8%, and losses from inverse Comptonisation are negligible).

For the synchrotron-dominated fit, radiative losses from synchrotron cooling are therefore not negligible in the X-ray waveband. This means that the initial particle spectrum (at lower γ_e) must be harder than $p \sim 3$. That is, the spectrum should initially have $p \sim 2$ (since the particle index should change by $\Delta p \sim 1$ above and below the synchrotron cooling break), and then the spectrum would soften to $p \sim 3$ at higher electron Lorentz factors when synchrotron cooling becomes significant. This effect on the shape of the particle spectrum is not included in the MNW05 model, which assumes that adiabatic losses always dominate (we note, however, that some of this spectral evolution could be “hidden” by the optically thick portion of the jet). The MNW05 model also assumes that the particle spectrum is similar across the entire outer jet. That assumption was motivated by multi-wavelength campaigns on jets from active galactic nuclei (where the evolution of the spectral index can be spatially resolved along the jet) that do not show spectral evolution over distances much greater than the cooling lengths (e.g., Jester et al. 2001). However, since we cannot spatially resolve BHXB jets in quiescence, we cannot directly test this assumption via observations of J1118.

Despite the above, we can still draw some qualitative conclusions from the synchrotron-dominated fit (i.e., in the case that particle acceleration is efficient and X-rays are synchrotron cooled). In this case, the synchrotron cooling break

must fall below the X-ray waveband. If the cooling break falls above the IR waveband (i.e., at frequencies above the jet break ν_b), then the optically thin synchrotron emission would initially have a flatter spectral index between the jet break and the cooling break. That implies that ν_b should fall at a lower frequency than shown in Figure 2. In turn, there is less room for the jet to account for any IR-excess, making the idea of a circumbinary disk more likely.⁷ However, the above is only one possibility, as it could instead be the case that the synchrotron cooling break falls below the IR band and within the optically thick portion of the jet. In that case, the synchrotron contribution to the IR band from the non-thermal electrons would not change by a large amount. Unfortunately, we cannot draw strong quantitative conclusions (besides our concerns on the quality of the model fit, we also must bear in mind that our IR constraints are non-simultaneous). However, we do note that the above issues do not affect the properties of the jet base, and they therefore do not alter our conclusions at the beginning of Section 5.

So far, our hesitation to favor the synchrotron dominated fit is primarily due to a concern that the fit approaches a parameter space that is inconsistent with some of the underlying assumptions behind the MNW05 model. However, the synchrotron cooled X-ray scenario becomes slightly less appealing when also considering our results on the radio/X-ray luminosity correlation in Gallo et al. (2014). With the new data point of J1118 in quiescence (at $L_X/L_{\text{Edd}} \sim 10^{-8.5}$), Gallo et al. (2014) demonstrate that J1118 exhibits a tight, non-linear radio/X-ray luminosity correlation over five decades in X-ray luminosity, of the form $L_r \propto L_X^{0.72 \pm 0.09}$. The slope of the non-linear correlation is suggestive of radiatively inefficient X-ray processes. More specifically, to explain this slope, the X-ray luminosity should scale approximately quadratically (depending on the radio spectral index) with the normalized mass accretion rate $\dot{m} = \dot{M}/\dot{M}_{\text{Edd}}$ (e.g., Markoff et al. 2003). However, synchrotron cooled emission from non-thermal electrons scales linearly with \dot{m} (e.g., Heinz 2004), which would result in a steeper luminosity correlation with a slope almost twice as large (Heinz 2004; Yuan & Cui 2005). So, if J1118 were to transition from radiatively inefficient X-rays in the low-hard state to synchrotron cooled X-rays in quiescence, as would be implied by the synchrotron-dominated fit, then the slope of its radio/X-ray luminosity correlation should also steepen in quiescence (Yuan & Cui 2005). We do not observe such a steepening of the slope in the radio–X-ray luminosity plane. Therefore, in order for the synchrotron-dominated fit to be correct, the X-rays would have to transition to being synchrotron cooled at relatively low luminosities (so that the steepening of the slope is not noticeable even at $L_{\text{Edd}} \sim 10^{-8.5}$), or the expected scalings of radio and X-ray luminosity depend on other parameters in addition to \dot{m} .

We conclude that the SSC-dominated fit is likely a more believable representation of the data, in the context of the MNW05 model. However, we again stress that the above

concerns are only relevant to the post-acceleration jet zones and *not* the jet base or nozzle. Therefore, despite the above, we still consider our qualitative results that the nozzle becomes smaller and cooler in quiescence to be robust. To properly investigate the feasibility of efficient particle acceleration (i.e., high t_{acc}^{-1} and high $\gamma_{e,\text{max}}$) and synchrotron cooled X-rays would require adjustments to the model out of the scope of this paper (see Yuan & Cui 2005 for the application of a jet model including synchrotron cooling losses to an optical/UV/X-ray SED of J1118 in quiescence). We also stress that this issue is not a concern for the SSC-dominated fit. For the SSC-dominated fit, particle acceleration is very weak ($\gamma_{e,\text{max}} \sim 147$) and the magnetic field is smaller, so that adiabatic losses always dominate, consistent with our assumptions. Therefore, we are more confident in the physical parameters found by the SSC-dominated fit, provided that the X-rays indeed are predominantly SSC emission from a relativistic distribution of thermal electrons. Unfortunately, it is not trivial to predict the expected radio/X-ray correlation if BHXBs switch to SSC-dominated X-rays from a thermal electron population, so it is unclear at this point whether the SSC-dominated fit is consistent with the Gallo et al. (2014) non-linear correlation. We expand more on the SSC-dominated fit in the next subsection.

5.2 Jets in Quiescence

We begin this section by comparing similarities between our jet model and other types of accretion flows, in order to highlight robust results. McClintock et al. (2003) undertook an optical, UV, and X-ray campaign on J1118 in quiescence in 2002, for which they use an advection dominated accretion flow (ADAF; Ichimaru 1977; Narayan & Yi 1994; Abramowicz et al. 1995) to explain the X-ray spectrum. An ADAF is a type of RIAF, where the black hole is fed by a radiatively inefficient two-temperature plasma with very weak Coulomb coupling between ions. The radiative cooling timescale is longer than the free fall time into the black hole, resulting in under-luminous X-rays compared to a standard thin accretion disk, and a large fraction of accretion energy is advected directly into the black hole.⁸ Even without including an outflow, or with the benefit of radio constraints, McClintock et al. (2003) conclude that the X-rays are emitted via SSC (at least for $\lesssim 100$ keV photons; see Esin, McClintock & Narayan 1997) by a population of hot electrons, and they speculate that a non-thermal electron component could also be relevant. Of course, a major difference between the ADAF model and our jet model is that the jet model explicitly attributes the X-ray emission

⁷ We note that the NIR-optical emission is still dominated by the companion star. The synchrotron contribution to the UV emission would unlikely change much, since the UV is dominated by the thermal jet base.

⁸ Note that ADAFs are prone to developing various types of instabilities (e.g., Narayan & Yi 1995), and other variants of RIAFs are also possible (one example is the convection-dominated accretion flow, CDAF; Narayan, Igumenshchev & Abramowicz 2000; Quataert & Gruzinov 2000). In particular, as illustrated by the adiabatic inflow-outflow solution (ADIOS; Blandford & Begelman 1999), it is very plausible that a significant fraction of the accretion energy is instead carried away as mechanical energy in the form of an outflow, and not advected directly into the black hole (also see e.g., Fender, Gallo & Jonker 2003, and references therein, for the role that an outflow may play).

to an outflowing quasi-thermal component. Also, an attractive feature of jet models is that the outflow self-consistently explains the radio emission, since the physical conditions at the base of the jet (responsible for the optical/UV thermal synchrotron and X-ray SSC) determine the properties in the outer regions of the outflow (responsible for the radio emission). Yuan & Cui (2005) applied a hybrid ADAF/jet model to the SED from McClintock et al. (2003), and they also prefer jet-dominated X-rays in quiescence (although they argue for synchrotron from non-thermal electrons).

According to the SSC-dominated fit, our main conclusion is that the outer jet of J1118 experiences less efficient particle acceleration in quiescence compared to the hard state (i.e., the accelerated non-thermal electron tail does not reach high Lorentz factors). This conclusion is consistent with the picture described for Sgr A* in Section 1 (which also appears to undergo weaker particle acceleration and have a non-thermal SSC contribution to the quiescent X-rays; e.g., Falcke & Markoff 2000; Markoff et al. 2001). A similar conclusion was also reached for A0620-00 in quiescence, for which the same jet model converged toward similar best-fit parameters as we find for J1118 (Gallo et al. 2007). Furthermore, the BHXB Swift J1357.2-0933 was recently suggested to have the lowest quiescent X-ray luminosity of any known BHXB (Armas Padilla et al. 2014), making it suitable for comparisons to J1118 and A0620-00. Swift J1357.2-0933 has a very steep NIR-optical spectrum ($\alpha_\nu = -1.4$) in quiescence, which is also consistent with synchrotron radiation from a thermal distribution of electrons in a weak jet (Shahbaz et al. 2013). Thus, the best-fit model for J1118 in Figure 1 may indeed represent the baseline accretion/jet properties for quiescent black holes.

We note that the best-fit k -values are fairly low for the SSC-dominated fit. That could cause some concern, because a very small magnetic energy might violate the assumption in the MNW05 model of a maximally dominated jet. However, the mechanism(s) in which energy redistributes itself in the jet launching zone (i.e., the nozzle) are not well understood, so it is difficult for us to quantify if the small k values are unphysical or not. It is potentially interesting that the best-fit to A0620-00 in quiescence with the same model also prefers a small- k (Gallo et al. 2007); the small equipartition between magnetic field and electron energy densities could therefore be hinting at an interesting phenomenological property of quiescent black holes worth focusing on in the future.

Considering the above (and in the context of the SSC-dominated fit), it could be the case that an important difference between quiescent and hard state BHXBs is the degree to which an accelerated electron component contributes to the high-energy radiation. As BHXBs fade into quiescence, the jet base becomes less magnetically dominated, cooler, and more compact, and the maximum energy of any accelerated electrons becomes smaller. The net result may be a weaker outflow that does not develop the necessary structures to efficiently accelerate particles (see, e.g., Polko, Meier & Markoff 2010). The X-rays in turn switch from being a combination of optically thin synchrotron emission (e.g., Markoff, Falcke & Fender 2001; Plotkin et al. 2012) and/or emission associated with the hot flow (e.g., Esin et al. 2001; Yuan et al. 2005) in the hard state, to becoming dominated by SSC off the outflowing

(quasi)-thermal jet in quiescence. Such a switch could also be the cause of the observed X-ray spectral softening as a BHXB transitions from the hard state into quiescence (Plotkin, Gallo & Jonker 2013). If all BHXB accretion flows and jets evolve toward a similar baseline in quiescence, then it may also be natural to expect diverse accretion properties in the hard state (depending on the strength of the non-thermal electron component). For example, for J1118, the slope of the NIR-optical spectrum in the *hard* state has been observed to range from very steep ($\alpha_\nu \sim -1.4$; Russell et al. 2013) to values more typical of optically thin synchrotron radiation ($\alpha_\nu \sim -0.8$; Hynes et al. 2006; Russell et al. 2013) at different epochs, which could be reflecting different levels of particle acceleration. In addition to the above arguments that BHXBs eventually reach a quiescent baseline, the idea for less variety in quiescence might also be supported by multiwavelength observations that track transient BHXBs through the radio/X-ray luminosity plane as they fade into quiescence following an outburst (e.g., Jonker et al. 2010, 2012; Ratti et al. 2012). To test the above idea further, it would be helpful to have a prediction on the expected slope of radio/X-ray luminosity correlations if X-rays are dominated by SSC (from a thermal electron distribution), and also more simultaneous radio and X-ray constraints on highly quiescent black holes (to learn if all quiescent black holes have similar radio to X-ray flux ratios).

6 SUMMARY

The recent detection of radio emission from J1118 deep in quiescence (Gallo et al. 2014) provides new, much needed constraints on accretion flows and their jets at the lowest detectable Eddington ratios ($L_X \sim 10^{-8.5} L_{\text{Edd}}$). Currently, the only other BHXB with a radio detection and well-sampled SED at such a low Eddington ratio is A0620-00 (Gallo et al. 2006, 2007). From the combination of both sources, we can start to lay a foundation to ultimately learn if all quiescent BHXBs have similar accretion properties, if relativistic jets always persist at the lowest detectable Eddington ratios, and the degree to which accelerated non-thermal electrons are energetically important. These constraints are relevant across the entire black hole mass scale, as most SMBHs also likely accrete in the quiescent regime (if they are not completely dormant).

We undertook a coordinated multiwavelength campaign to assemble a broadband spectrum for J1118 in quiescence, including radio (VLA), NIR/optical (WHT), UV (Swift), and X-ray (Chandra) observations. We then applied a multi-zone jet model to the broadband spectrum (Markoff, Nowak & Wilms 2005) to constrain the physical parameters of the system, and to tease out the dominant emission mechanism(s) in each waveband. The same model has also been applied to A0620-00 in quiescence (Gallo et al. 2007) and to J1118 at higher luminosities in the hard state (Maitra et al. 2009), allowing us to make uniform comparisons.

We can adequately model the entire spectrum by including radiation only from the outflowing jet, and flux from the companion star. As in the hard state, the radio emission is attributed to the sum of multiple zones of self-absorbed synchrotron emission from the outer jet (e.g.,

Blandford & Königl 1979). As J1118 fades into quiescence, we determine that its jet base becomes more compact (by up to an order of magnitude) and slightly cooler (by at least a factor of two). Meanwhile, in our preferred model fit, the jet base also becomes less magnetically dominated, and particle acceleration becomes less efficient (i.e., non-thermal electrons in the outer regions of the jet do not attain high Lorentz factors). Ignoring the companion star, the optical/UV emission is thermal synchrotron emission from a mildly relativistic population of quasi-thermal electrons in the jet base, and the X-rays are corresponding SSC. The particle acceleration is too weak for non-thermal electrons to contribute significant amounts of high-energy radiation. We do not require a circumbinary disk (e.g., Munro & Mauerhan 2006) in the IR, or thermal emission from the outer disk in the optical/UV, but in reality both components could contribute emission at some level.

The above scenario is consistent with results on A0620-00, and also with broadband modeling of Sgr A* (using a similar jet model; e.g., Falcke & Markoff 2000; Markoff et al. 2001). We thus speculate that J1118 and A0620-00 could represent a canonical baseline for quiescent black hole accretion flows and jets. The overall structure could also be similar for hard state BHXBs. However, at higher luminosities, there is likely an increased flux of disk seed photons near the jet base for external inverse Compton scattering, and reflection off the accretion disk will also be more important. The primary difference inferred from our work might also be the degree to which hard state jets can accelerate a non-thermal tail of electrons. With stronger acceleration, non-thermal particles may contribute more radiation to the high-energy wavebands.

In the future, well-sampled SEDs for more quiescent BHXBs are clearly needed, which can currently be obtained only for very nearby (and ideally high Galactic latitude) systems. In particular, additional high-resolution UV spectra (e.g., with COS on HST) would be helpful for constraining the disk contribution to the UV (e.g., Froning et al. 2011). Observational constraints on the high-energy cutoff would also be extremely useful, for which coordinated UV and X-ray observations (of unabsorbed systems) could be a promising avenue. Curvature between the UV and X-ray band could be indicative of a cooling break. Hard X-ray constraints would also be useful if the high-energy cutoff falls at hard X-ray energies. Besides the high-energy cutoff, the other poorly constrained parameter from the jet model is the location of the jet acceleration zone, z_{acc} , which is important for understanding the jet's energetics. Improving constraints on z_{acc} requires more coverage from the sub-mm through IR, which could be achieved with ALMA for some sources, and/or the James Webb Space Telescope in the future. We note that, while we await such observations, there is already a positive outlook to more tightly constrain quiescent jet properties (with current data) through improvements in the theoretical modeling. The next generation of the jet model employed here will self-consistently derive the flow solution from the jet base to acceleration zone (z_{acc}) for a given set of initial conditions in the inner accretion flow (Polko, Meier & Markoff 2010, 2013, 2014), which will significantly reduce the number of free parameters.

ACKNOWLEDGMENTS

We thank Marianne Heida for her help with the reduction of the NIR WHT images, and we thank Neil Gehrels and the Swift team for approving and scheduling the Swift/UVOT observations. Support for this work was provided by the National Aeronautics and Space Administration through Chandra Award Number GO3-14036X issued by the Chandra X-ray Observatory Center, which is operated by the Smithsonian Astrophysical Observatory for and on behalf of the National Aeronautics Space Administration under contract NAS8-03060. JMJ is supported by an Australian Research Council (ARC) Future Fellowship (FT140101082) and also acknowledges support from an ARC Discovery Grant (DP120102393). SD acknowledges funding support from the French Research National Agency: CHAOS project ANR-12-BS05-0009. This research has made use of software provided by the Chandra X-ray Center (CXC) in the application package CIAO. The William Herschel Telescope is operated on the island of La Palma by the Isaac Newton Group in the Spanish Observatorio del Roque de los Muchachos of the Instituto de Astrofísica de Canarias. The National Radio Astronomy Observatory is a facility of the National Science Foundation operated under cooperative agreement by Associated Universities, Inc. This publication makes use of data products from the Wide-field Infrared Survey Explorer, which is a joint project of the University of California, Los Angeles, and the Jet Propulsion Laboratory/California Institute of Technology, funded by the National Aeronautics and Space Administration. This work is based in part on archival data obtained with the Spitzer Space Telescope, which is operated by the Jet Propulsion Laboratory, California Institute of Technology under a contract with NASA.

REFERENCES

- Abramowicz M. A., Chen X., Kato S., Lasota J.-P., Regev O., 1995, *ApJ*, 438, L37
- Armas Padilla M., Wijnands R., Degenaar N., Muñoz-Díaz T., Casares J., Fender R. P., 2014, *MNRAS*, 444, 902
- Belloni T. M., 2010, in *Lecture Notes in Physics*, Berlin Springer Verlag, Vol. 794, *Lecture Notes in Physics*, Berlin Springer Verlag, Belloni T., ed., p. 53
- Bernardini F., Cackett E. M., 2014, *MNRAS*, 439, 2771
- Blandford R. D., Begelman M. C., 1999, *MNRAS*, 303, L1
- Blandford R. D., Königl A., 1979, *ApJ*, 232, 34
- Brockopp C., Jonker P. G., Maitra D., Krimm H. A., Pooley G. G., Ramsay G., Zurita C., 2010, *MNRAS*, 404, 908
- Cardelli J. A., Clayton G. C., Mathis J. S., 1989, *ApJ*, 345, 245
- Cash W., 1979, *ApJ*, 228, 939
- Chaty S., Haswell C. A., Malzac J., Hynes R. I., Shrader C. R., Cui W., 2003, *MNRAS*, 346, 689
- Corbel S., Fender R. P., 2002, *ApJ*, 573, L35
- Corbel S., Koerding E., Kaaret P., 2008, *MNRAS*, 389, 1697
- Corbel S., Tomsick J. A., Kaaret P., 2006, *ApJ*, 636, 971
- Dhawan V., Mirabel I. F., Rodríguez L. F., 2000, *ApJ*, 543, 373
- Dibi S., Markoff S., Belmont R., Malzac J., Barriere N. M., Tomsick J. A., 2014, *MNRAS*, 441, 1005

- Dodds-Eden, K., Porquet, D., Trap, G., et al. 2009, *ApJ*, 698, 676
- Drury, L. O. 1983, *Reports on Progress in Physics*, 46, 973
- Esin A. A., McClintock J. E., Drake J. J., Garcia M. R., Haswell C. A., Hynes R. I., Munro M. P., 2001, *ApJ*, 555, 483
- Esin A. A., McClintock J. E., Narayan R., 1997, *ApJ*, 489, 865
- Falcke, H., & Biermann, P. L. 1995, *A&A*, 293, 665
- Falcke H., Markoff S., 2000, *A&A*, 362, 113
- Fazio G. G., Hora J. L., Allen L. E. et al., 2004, *ApJS*, 154, 10
- Fender R. P., 2001, *MNRAS*, 322, 31
- Fender R. P., Gallo E., Jonker P. G., 2003, *MNRAS*, 343, L99
- Froning C. S., Cantrell A. G., Maccarone T. J. et al., 2011, *ApJ*, 743, 26
- Fruscione A., McDowell J. C., Allen G. E. et al., 2006, in *Society of Photo-Optical Instrumentation Engineers (SPIE) Conference Series*, Vol. 6270, *Society of Photo-Optical Instrumentation Engineers (SPIE) Conference Series*
- Gallo E., Fender R., Kaiser C., Russell D., Morganti R., Oosterloo T., Heinz S., 2005, *Nat*, 436, 819
- Gallo E., Fender R. P., Hynes R. I., 2005, *MNRAS*, 356, 1017
- Gallo E., Fender R. P., Miller-Jones J. C. A., Merloni A., Jonker P. G., Heinz S., Maccarone T. J., van der Klis M., 2006, *MNRAS*, 370, 1351
- Gallo E., Migliari S., Markoff S., Tomsick J. A., Bailyn C. D., Berta S., Fender R., Miller-Jones J. C. A., 2007, *ApJ*, 670, 600
- Gallo E., et al., 2014, *MNRAS*, 445, 290
- Garmire G. P., Bautz M. W., Ford P. G., Nousek J. A., Ricker, Jr. G. R., 2003, in *Society of Photo-Optical Instrumentation Engineers (SPIE) Conference Series*, Vol. 4851, *X-Ray and Gamma-Ray Telescopes and Instruments for Astronomy*, Truemper J. E., Tananbaum H. D., eds., pp. 28–44
- Gehrels N., Chincarini G., Giommi P. et al., 2004, *ApJ*, 611, 1005
- Gelino D. M., Balman Ş., Kızıloğlu Ü., Yılmaz A., Kalemci E., Tomsick J. A., 2006, *ApJ*, 642, 438
- Heinz S., 2004, *MNRAS*, 355, 835
- Hjellming R. M., Johnston K. J., 1988, *ApJ*, 328, 600
- Hjellming R. M., Rupen M. P., Mioduszewski A. J., Narayan R., 2000, *The Astronomer's Telegram*, 54, 1
- Houck J. C., Denicola L. A., 2000, in *Astronomical Society of the Pacific Conference Series*, Vol. 216, *Astronomical Data Analysis Software and Systems IX*, Manset N., Veillet C., Crabtree D., eds., p. 591
- Hynes R. I., Bradley C. K., Rupen M., Gallo E., Fender R. P., Casares J., Zurita C., 2009, *MNRAS*, 399, 2239
- Hynes R. I., Haswell C. A., Cui W. et al., 2003, *MNRAS*, 345, 292
- Hynes R. I., Mauche C. W., Haswell C. A., Shrader C. R., Cui W., Chaty S., 2000, *ApJL*, 539, L37
- Hynes R. I., Robinson E. L., 2012, *ApJ*, 749, 3
- Hynes R. I., Robinson E. L., Pearson K. J. et al., 2006, *ApJ*, 651, 401
- Ichimaru S., 1977, *ApJ*, 214, 840
- Jester, S., Röser, H.-J., Meisenheimer, K., Perley, R., & Conway, R. 2001, *A&A*, 373, 447
- Jokipii J. R., 1987, *ApJ*, 313, 842
- Jonker P. G., Miller-Jones J., Homan J. et al., 2010, *MNRAS*, 401, 1255
- Jonker P. G., Miller-Jones J. C. A., Homan J., Tomsick J., Fender R. P., Kaaret P., Markoff S., Gallo E., 2012, *MNRAS*, 423, 3308
- Kataoka J., Madejski G., Sikora M. et al., 2008, *ApJ*, 672, 787
- Khargharia J., Froning C. S., Robinson E. L., Gelino D. M., 2013, *AJ*, 145, 21
- Kong A. K. H., McClintock J. E., Garcia M. R., Murray S. S., Barret D., 2002, *ApJ*, 570, 277
- Kubota A., Tanaka Y., Makishima K., Ueda Y., Dotani T., Inoue H., Yamaoka K., 1998, *PASJ*, 50, 667
- Maitra D., Markoff S., Brocksopp C., Noble M., Nowak M., Wilms J., 2009, *MNRAS*, 398, 1638
- Malzac J., Merloni A., Fabian A. C., 2004, *MNRAS*, 351, 253
- Markoff S., 2005, *ApJL*, 618, L103
- Markoff S., Falcke H., Fender R., 2001, *A&A*, 372, L25
- Markoff S., Falcke H., Yuan F., Biermann P. L., 2001, *A&A*, 379, L13
- Markoff S., Nowak M., Corbel S., Fender R., Falcke H., 2003, *A&A*, 397, 645
- Markoff S., Nowak M., Young A. et al., 2008, *ApJ*, 681, 905
- Markoff S., Nowak M. A., Wilms J., 2005, *ApJ*, 635, 1203
- McClintock J. E., Haswell C. A., Garcia M. R. et al., 2001, *ApJ*, 555, 477
- McClintock J. E., Horne K., Remillard R. A., 1995, *ApJ*, 442, 358
- McClintock J. E., Narayan R., Garcia M. R., Orosz J. A., Remillard R. A., Murray S. S., 2003, *ApJ*, 593, 435
- McMullin J. P., Waters B., Schiebel D., Young W., Golap K., 2007, in *Astronomical Society of the Pacific Conference Series*, Vol. 376, *Astronomical Data Analysis Software and Systems XVI*, Shaw R. A., Hill F., Bell D. J., eds., p. 127
- Migliari, S., Tomsick, J. A., Markoff, S., et al. 2007, *ApJ*, 670, 610
- Miller J. M., Homan J., Steeghs D., Rupen M., Hunstead R. W., Wijnands R., Charles P. A., Fabian A. C., 2006, *ApJ*, 653, 525
- Miller-Jones J. C. A., Jonker P. G., Maccarone T. J., Nelemans G., Calvelo D. E., 2011, *ApJL*, 739, L18
- Mukai K., 1993, *Legacy*, vol. 3, p.21-31, 3, 21
- Munro M. P., Mauerhan J., 2006, *ApJL*, 648, L135
- Narayan R., Igumenshchev I. V., Abramowicz M. A., 2000, *ApJ*, 539, 798
- Narayan R., Yi I., 1994, *ApJL*, 428, L13
- Narayan R., Yi I., 1995, *ApJ*, 444, 231
- Plotkin R. M., Gallo E., Jonker P. G., 2013, *ApJ*, 773, 59
- Plotkin R. M., Markoff S., Kelly B. C., Körding E., Anderson S. F., 2012, *MNRAS*, 419, 267
- Polko P., Meier D. L., Markoff S., 2010, *ApJ*, 723, 1343
- Polko P., Meier D. L., Markoff S., 2013, *MNRAS*, 428, 587
- Polko P., Meier D. L., Markoff S., 2014, *MNRAS*, 438, 959
- Quataert E., Gruzinov A., 2000, *ApJ*, 539, 809
- Ratti E. M., Jonker P. G., Miller-Jones J. C. A. et al., 2012, *MNRAS*, 423, 2656
- Reis R. C., Fabian A. C., Miller J. M., 2010, *MNRAS*, 402, 836

- Remillard R. A., McClintock J. E., 2006, *AR&A*, 44, 49
- Reynolds M. T., Miller J. M., 2013, *ApJ*, 769, 16
- Reynolds M. T., Reis R. C., Miller J. M., Cackett E. M., Degenaar N., 2014, *MNRAS*, 441, 3656
- Rieke G. H., Young E. T., Engelbracht C. W. et al., 2004, *ApJS*, 154, 25
- Roming P. W. A., Kennedy T. E., Mason K. O. et al., 2005, *Space Science Reviews*, 120, 95
- Russell D. M., Maitra D., Dunn R. J. H., Markoff S., 2010, *MNRAS*, 405, 1759
- Russell D. M., Markoff S., Casella P. et al., 2013, *MNRAS*, 429, 815
- Schirmer M., 2013, *ApJS*, 209, 21
- Shahbaz T., Russell D. M., Zurita C., Casares J., Corral-Santana J. M., Dhillon V. S., Marsh T. R., 2013, *MNRAS*, 434, 2696
- Skrutskie M. F., Cutri R. M., Stiening R. et al., 2006, *AJ*, 131, 1163
- Stirling A. M., Spencer R. E., de la Force C. J., Garrett M. A., Fender R. P., Ogle R. N., 2001, *MNRAS*, 327, 1273
- Tomsick J. A., Corbel S., Fender R. et al., 2003, *ApJL*, 597, L133
- Torres M. A. P., Callanan P. J., Garcia M. R., Zhao P., Laycock S., Kong A. K. H., 2004, *ApJ*, 612, 1026
- Vila, G. S., Romero, G. E., & Casco, N. A. 2012, *A&A*, 538, A97
- Wang X., Wang Z., 2014, *ApJ*, 788, 184
- Wilkinson T., Uttley P., 2009, *MNRAS*, 397, 666
- Wright E. L., Eisenhardt P. R. M., Mainzer A. K. et al., 2010, *AJ*, 140, 1868
- York D. G., Adelman J., Anderson, Jr. J. E. et al., 2000, *AJ*, 120, 1579
- Yuan, F., Cui, W., & Narayan, R. 2005, *ApJ*, 620, 905
- Yuan F., Cui W., 2005, *ApJ*, 629, 408
- Yuan F., Markoff S., Falcke H., 2002, *A&A*, 383, 854
- Zhang, J.-F., & Xie, F.-G. 2013, *MNRAS*, 435, 1165
- Zurita C., Torres M. A. P., Steeghs D. et al., 2006, *ApJ*, 644, 432

This paper has been typeset from a \LaTeX file prepared by the author.